arXiv:2111.01152v3 [cond-mat.str-el] 9 Aug 2022

Topological Phases in AB-Stacked $MoTe_2/WSe_2$: $\mathbb{Z}_2$ Topological Insulators, Chern Insulators, and Topological Charge Density Waves

Haining Pan,[1] Ming Xie,[1] Fengcheng Wu,[2,3,*] and Sankar Das Sarma[1]

[1] *Condensed Matter Theory Center and Joint Quantum Institute, Department of Physics, University of Maryland, College Park, Maryland 20742, USA*
[2] *School of Physics and Technology, Wuhan University, Wuhan 430072, China*
[3] *Wuhan Institute of Quantum Technology, Wuhan 430206, China*

We present a theory on the quantum phase diagram of AB-stacked $MoTe_2/WSe_2$ using a self-consistent Hartree-Fock calculation performed in the plane-wave basis, motivated by the observation of topological states in this system. At filling factor $\nu = 2$ (two holes per moiré unit cell), Coulomb interaction can stabilize a $\mathbb{Z}_2$ topological insulator by opening a charge gap. At $\nu = 1$, the interaction induces three classes of competing states, spin density wave states, an in-plane ferromagnetic state, and a valley polarized state, which undergo first-order phase transitions tuned by an out-of-plane displacement field. The valley polarized state becomes a Chern insulator for certain displacement fields. Moreover, we predict a topological charge density wave forming a honeycomb lattice with ferromagnetism at $\nu = 2/3$. Future directions on this versatile system hosting a rich set of quantum phases are discussed.

Introduction.— Topological phases of matter have been among the most active and important research areas in condensed matter physics ever since the experimental discovery of the quantum Hall effect [1] in the presence of strong magnetic fields. The mechanism of the quantum Hall effect, especially the quantization of Hall conductance, has been understood in terms of the topological invariant of the Chern number [2, 3]. The concept of quantum Hall insulators has been generalized to quantum anomalous Hall insulators (also known as Chern insulators) [4] and quantum spin Hall insulators (also known as $\mathbb{Z}_2$ topological insulators) [5], where the former exhibits quantized Hall effect without the external magnetic field, and the latter is the topological state in the presence of time-reversal symmetry. Among the extensive topological theoretical predictions [6–20], only a limited number of systems have so far been studied experimentally manifesting unambiguous topological invariants: Chern insulators have been realized in magnetically doped topological insulator thin films [21, 22], few-layer $MnBi_2Te_4$ [23, 24], and graphene-based moiré materials [25–29], and transport signatures of the quantum spin Hall effect have been reported in HgTe quantum wells [30], InAs/GaSb quantum wells [31, 32] and monolayer WTe_2 [33, 34].

The recent advent of moiré materials, followed by the discovery of correlated insulators and superconductors in magic-angle twisted bilayer graphene [35, 36], provides vast new opportunities to design different phases of matter, including the topological phases discussed above [25–27, 37–47]. It was theoretically proposed [48] that moiré bands in twisted transition metal dichalcogenide homobilayers can be mapped to the Kane-Mele model [48–50]. Coulomb repulsion can further drive broken symmetry insulating states (e.g., Chern insulators) because the topological moiré bands have narrow bandwidth. This leads to interesting physics involving the interplay between band topology and strong correlations. A recent experiment on AB-stacked $MoTe_2/WSe_2$ [51] reported well-developed quantum anomalous Hall effect at filling factor $\nu = 1$, and possible evidence for quantum spin Hall effect at $\nu = 2$. This experiment is unprecedented, as it demonstrates experimentally that quantum anomalous Hall and quantum spin Hall effects could be realized in a single system, something that has never happened before as the two phenomena are quite distinct. It is also surprising, as it utilizes a heterobilayer instead of the homobilayer proposed in Ref. 48 for the manifestation of Transition Metal Dichalcogenides (TMD) topology. The surprising rich phenomena observed in $MoTe_2/WSe_2$ calls for detailed theoretical studies [52–54].

In this Letter, we present a topological theoretical study of interacting AB-stacked $MoTe_2/WSe_2$. The single-particle physics is described by a continuum moiré Hamiltonian that incorporates the topmost valence bands from both layers. An out-of-plane displacement field tunes the band offset between the two layers, and drives a topological phase transition for the first moiré valence band. The Coulomb interaction is treated using a self-consistent Hartree-Fock approximation *without* the bias of projecting it to a few selected moiré bands. Our main results are summarized as follows. (1) At $\nu = 2$, the single-particle band structure predicts a metallic state in the topological regime, but the Coulomb interaction can open up a gap, and therefore, stabilize the $\mathbb{Z}_2$ topological insulator. (2) At $\nu = 1$, we obtain a rich quantum phase diagram that includes three classes of competing phases, spin density wave states, an in-plane ferromagnetic state, and a valley polarized state. The valley polarized state becomes a Chern insulator for a certain range of displacement fields. (3) At the fractional filling factor $\nu = 2/3$, we predict a topological density wave state, and identify the condition for its experimental realization.

Our results provide a consistent mean-field description

of the experimental observations (along with new predictions) in Ref. 51, which is an important step toward a full understanding of quantum phases in the moiré TMD physics. In a broader perspective, our work establishes affirmatively that the interplay between many-body interaction and single-particle band topology can induce a rich set of distinct topological phases (e.g., quantum anomalous Hall insulators and quantum spin Hall insulators) within one realistic system.

Model.— We focus on AB-stacked $MoTe_2/WSe_2$ with an exact 180° twist angle. The moiré superlattices have the C_{3v} point group symmetry and a moiré period $a_M = a_\mathfrak{b}a_\mathfrak{t}/|a_\mathfrak{b} - a_\mathfrak{t}|$, where $(a_\mathfrak{b}, a_\mathfrak{t})$=(3.575Å, 3.32Å) are the lattice constant of $MoTe_2$ and WSe_2, respectively. The large lattice constant mismatch makes the moiré superlattices relatively immune to twist angle disorder. As shown in Fig. 1 (a), there are three high-symmetry regions in one moiré unit cell, labeled as MM, XX, and MX, corresponding to local atomic configurations with C_{3z} (threefold rotational) symmetry.

The density functional theory calculation [51, 53] of AB-stacked $MoTe_2/WSe_2$ shows that states at the valence band edge originate from $\pm K$ valleys of $MoTe_2$, where $\pm K$ refer to corners of the monolayer Brillouin zone. Therefore, we focus on $\pm K$ valleys which are related by the $\mathcal{T}$ symmetry. For valence bands at the two valleys, there are large spin splittings that are both valley and layer dependent, as illustrated in Fig. 1 (b). By retaining the topmost valence bands from each layer, we construct [48, 49, 53] a valley-dependent continuum Hamiltonian as follows

$$H_\tau = \begin{pmatrix} -\frac{\hbar^2\boldsymbol{k}^2}{2m_\mathfrak{b}} + \Delta_\mathfrak{b}(\boldsymbol{r}) & \Delta_{\mathrm{T},\tau}(\boldsymbol{r}) \\ \Delta^\dagger_{\mathrm{T},\tau}(\boldsymbol{r}) & -\frac{\hbar^2(\boldsymbol{k}-\tau\boldsymbol{\kappa})^2}{2m_\mathfrak{t}} + \Delta_\mathfrak{t}(\boldsymbol{r}) + V_{z\mathfrak{t}} \end{pmatrix}, \tag{1}$$

where $\tau = \pm 1$ represents $\pm K$ valleys, and $\boldsymbol{\kappa} = \frac{4\pi}{3a_M}(1, 0)$ is at a corner of the moiré Brillouin zone. For each valley, the 2×2 Hamiltonian hybridizes the bottom layer ($\mathfrak{b}$) and top layer ($\mathfrak{t}$), where the off diagonal terms describe the interlayer tunneling $\Delta_{\mathrm{T},\tau}$, and the diagonal terms describe the momentum-shifted kinetic energy with the effective mass $(m_\mathfrak{b}, m_\mathfrak{t}) = (0.65, 0.35)m_e$ (m_e is the rest electron mass), plus the intralayer potential $\Delta_{\mathfrak{b}/\mathfrak{t}}$, and a band offset $V_{z\mathfrak{t}}$ [Fig. 1(b)]. Our H_τ differs from that in Ref. 53 by a gauge transformation.

The periodic potential $\Delta_\mathfrak{b}(\boldsymbol{r})$ is parametrized as

$$\Delta_\mathfrak{b}(\boldsymbol{r}) = 2V_\mathfrak{b} \sum_{j=1,3,5} \cos(\boldsymbol{g}_j \cdot \boldsymbol{r} + \psi_\mathfrak{b}), \tag{2}$$

where $V_\mathfrak{b}$ and $\psi_\mathfrak{b}$ respectively characterize the amplitude and spatial pattern of the potential, and $\boldsymbol{g}_j = \frac{4\pi}{\sqrt{3}a_M}\left(-\sin\frac{\pi(j-1)}{3}, \cos\frac{\pi(j-1)}{3}\right)$ are the moiré reciprocal lattice vectors in the first shell. We set $\Delta_\mathfrak{t}(\boldsymbol{r}) = 0$, since the low-energy physics only involves the band maximum

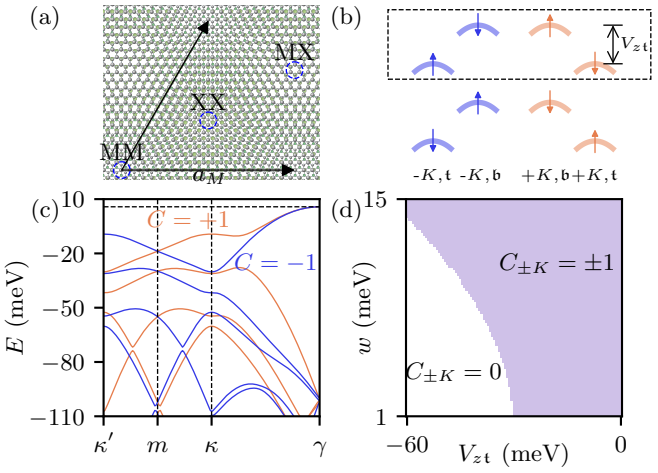


FIG. 1. (a) Moiré superlattice of AB-stacked $MoTe_2/WSe_2$. (b) A schematic plot for band alignment in the heterobilayer. Only states in the dashed box are retained in the Hamiltonian H_τ. (c) Single-particle moiré band structure with parameters $(w, V_\mathfrak{b}, V_{z\mathfrak{t}})$ =(12 meV, 7 meV, −20 meV). Orange (blue) lines show $+K(-K)$-valley moiré bands. The dashed line shows the Fermi energy of the charge neutrality. The first moiré valence band from $\pm K$ valleys carry ± 1 Chern number. (See the Supplemental Material [55][56–58] for the definition of high-symmetry points in the moiré Brillouin zone.) (d) Single-particle topological phase diagram of the first moiré valence band as a function of w and $V_{z\mathfrak{t}}$ with $V_\mathfrak{b}$=7 meV.

of WSe_2 [53]. The interlayer tunneling term is

$$\Delta_{\mathrm{T},\tau}(\boldsymbol{r}) = \tau w\left(1 + \omega^\tau e^{i\tau\boldsymbol{g}_2\cdot\boldsymbol{r}} + \omega^{2\tau}e^{i\tau\boldsymbol{g}_3\cdot\boldsymbol{r}}\right), \tag{3}$$

where w describes the tunneling strength, and $\omega = e^{i\frac{2\pi}{3}}$ following the C_{3z} symmetry [53]. The valley dependence of $\Delta_{\mathrm{T},\tau}$ is constrained by $\mathcal{T}$ symmetry. Here $\Delta_{\mathrm{T},\tau}$ couples states with opposite spins, which is symmetry allowed because the heterobilayer breaks the $z \to -z$ mirror symmetry. For parameters in H_τ, we take $\psi_\mathfrak{b} = -14°$ such that the potential maximum of $\Delta_\mathfrak{b}(\boldsymbol{r})$ is at the MM site [53]; $V_{z\mathfrak{t}}$ is a parameter that is experimentally controllable by an applied out-of-plane displacement field; $V_\mathfrak{b}$ and w are taken as theoretical parameters that can be adjusted to study different phases. We note that the interlayer tunneling strength w can be modified by pressure.

The low-energy moiré bands and their topology are tunable by $V_{z\mathfrak{t}}$. For the intrinsic band offset $V_{z\mathfrak{t}}$ that has a large negative value (~ -110 meV) [53], the topmost moiré valence band at each valley mainly derives from the $MoTe_2$ layer and can be described by a tight-binding model on a triangular lattice, which is topologically trivial. By reducing $|V_{z\mathfrak{t}}|$ with an external displacement field, the energy gap between the topmost moiré valence bands derived respectively from $MoTe_2$ and WSe_2 can close and then reopen. This band inversion enabled by the tunneling term $\Delta_{\mathrm{T},\tau}$ can lead to topological phase transitions.

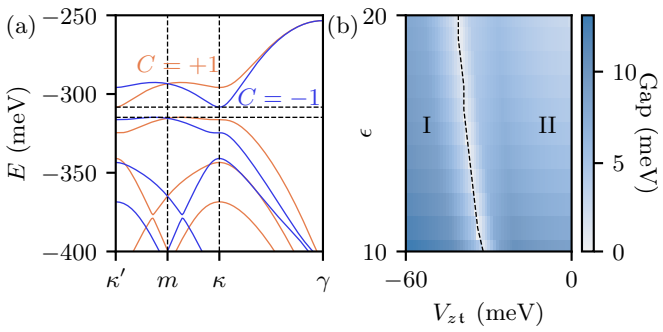


FIG. 2. (a) Band structure from the HF calculation at $\nu = 2$ with the same parameters as Fig. 1(c). Orange (blue) lines show $+K(-K)$-valley moiré bands. The two horizontal dashed lines identify the charge gap at $\nu = 2$. Here $\epsilon = 15$. (b) Charge gap at $\nu = 2$ from the HF calculation as a function of V_{zt} and ϵ. The gap vanishes at the dashed line, which separates phase I (topologically trivial insulators) and phase II ($\mathbb{Z}_2$ topological insulators). Here w=12 meV and $V_\mathfrak{b}$=7 meV.

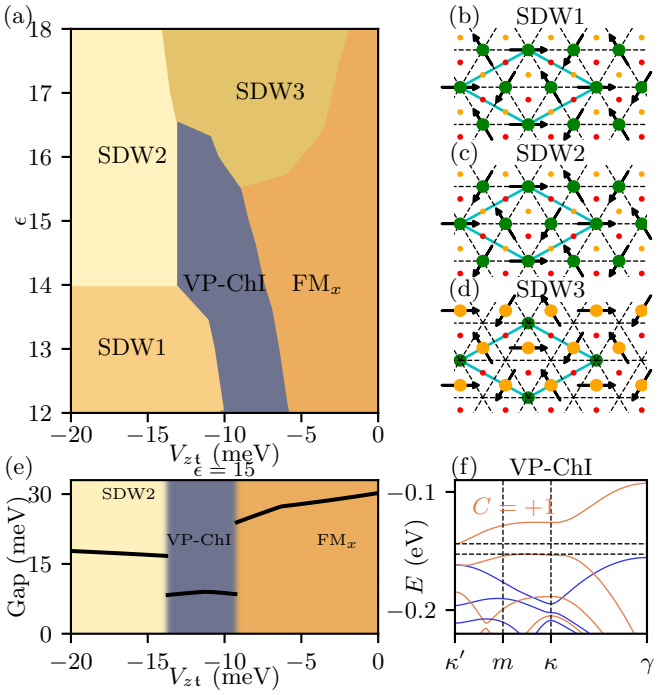


FIG. 3. (a) Interaction-induced phase diagram at $\nu = 1$ as a function of V_{zt} and ϵ. (b)-(d) Spin textures in the bottom layer for the three SDW states. The green, orange and red dots mark MM, XX and MX sites, respectively, where their sizes indicate the corresponding charge densities. (e) Charge gap at $\nu = 1$ as a function of V_{zt} with ϵ=15, w=12 meV, and $V_\mathfrak{b}$=7 meV. (f) Band structure of $\nu = 1$ VP ChI calculated using the HF method at $\epsilon = 15$ and $V_{zt} = -10$ meV. Orange (blue) lines show $+K(-K)$-valley moiré bands. The two horizontal dashed lines identify the charge gap at $\nu = 1$.

Figure 1(d) presents a topological phase diagram characterized by the valley-contrast Chern numbers $C_{\pm K}$ of the first moiré valence band in the parameter space of (V_{zt}, w). For V_{zt} above the critical value, $C_{\pm K}$ become nontrivial with value (± 1). Figure 1(c) plots a representative moiré band structure in the topologically nontrivial regime of Fig. 1(d). Note that there is no overall energy gap that separates the first and second moiré valence bands in Fig. 1(c). The effect of many-body interaction on this gap is crucial as studied in the following.

Coulomb Interactions.— The bandwidth of the first moiré valence band is on the order of $\hbar^2\boldsymbol{\kappa}^2/(2m_\mathfrak{b}) \approx 47$ meV, while the characteristic Coulomb interaction strength is on the order of $e^2/(\epsilon a_M) \approx 31$ meV for $a_M \approx 4.7$ nm and dielectric constant $\epsilon = 10$. Therefore, the Coulomb interaction has an energy scale comparable to the bandwidth [Fig. 1(c)], which puts the system in the strongly interacting regime with possible interaction-induced quantum phase transitions. We consider the dual-gate screened Coulomb interaction with the momentum-dependent potential $V(q) = 2\pi e^2 \tanh(qd)/(\epsilon q)$, where d is the gate-to-sample distance. We set $d = 5$ nm [51] unless otherwise stated. The dielectric constant ϵ is of the order of $10 - 20$, and we vary ϵ to illustrate how physical properties depend on the interaction strength.

We treat the Coulomb interaction using a self-consistent Hartree-Fock (HF) approximation applied to the continuum Hamiltonian in the plane-wave basis (see the Supplemental Material [55] for details). Here, we do *not* project the Coulomb interaction onto a few low-energy moiré bands, because it is generally not possible to identify a set of bands that are energetically isolated from other bands [Fig. 1(c)]. Our approach allows us to study interaction effects for different parameter regimes in a unified manner. We note that HF theory, although qualitatively reliable, may overestimate the tendency toward ordering, and may not be able to quantitatively capture the global phase diagram. Nevertheless, it is an important and nontrivial question of principle whether the experimental observations can be captured by a mean-field theory.

$\mathbb{Z}_2$ topological insulator at $\nu = 2$.— For the single-particle band structure shown in Fig. 1(c), $\nu = 2$ would correspond to a metallic state since there is no overall gap that separates the first and second moiré valence bands. However, after performing the self-consistent HF calculations using the same set of parameters, we find that a true gap develops at $\nu = 2$, as shown in Fig. 2(a). The first moiré valence band at each valley remains topologically nontrivial. Therefore, the $\nu = 2$ insulator in Fig. 2(a) belongs to the $\mathbb{Z}_2$ time-reversal invariant topological insulator as the $\mathbb{Z}_2$ topological invariant, defined in our case by $\mathrm{mod}[(C_{+K} - C_{-K})/2, 2]$ [5], is nontrivial given $C_{\pm K} = \pm 1$. This can be viewed as a realization of the interaction-induced quantum spin Hall insulator [5].

For generic parameter values, we present the topological phase diagram at $\nu = 2$ calculated using the HF approximation as a function of ϵ and V_{zt} in Fig. 2(b), where

there are two phases, the topologically trivial phase and the $\mathbb{Z}_2$ topological insulator phase, respectively for $V_{z\mathfrak{t}}$ below and above a critical value. At the critical $V_{z\mathfrak{t}}$, the charge gap vanishes. The critical $V_{z\mathfrak{t}}$ increases as ϵ decreases (Coulomb interaction increases) because a stronger Coulomb interaction opens a larger charge gap in the topologically trivial phase, which requires a larger displacement field to close the gap so that the topological phase transition can happen.

Competing phases at $\nu = 1$.— We study interaction-induced competing phases at $\nu = 1$ and show the quantum phase diagram in Fig. 3(a), which includes three distinct classes of states, a valley polarized (VP) state, spin density wave (SDW) states, and an in-plane ferromagnetic state (FM_x). We first describe the VP state, where the first moiré valence bands at $\pm K$ valleys have unequal occupations. Therefore, the VP state carries a finite out-of-plane spin polarization and spontaneously breaks $\mathcal{T}$ symmetry. Figure 3(f) shows a representative band structure calculated using the HF method for the VP state, which has a finite charge gap at $\nu = 1$ and realizes a Chern insulator (ChI) with a quantized Chern number 1. This gives rise to the VP-ChI phase in Fig. 3(a). The VP state may become topologically trivial for a large negative $V_{z\mathfrak{t}}$. However, such a VP *trivial* phase is absent in Fig. 3(a) because it is energetically unfavorable compared with SDW states for the parameter ranges used in this figure. To the other extreme ($V_{z\mathfrak{t}} \sim 0$), the VP state may become a metallic state that has partial valley polarization, though not energetically favorable compared with FM_x in Fig. 3(a).

We now turn to SDW and FM_x phases. The first moiré valence band in the topologically trivial regime of Fig. 1(d) can be described by a single-band tight-binding model on a triangular lattice, which, combined with the Coulomb interaction, realizes a generalized Hubbard model [59]. The single-band Hubbard model on a triangular lattice in the strong interaction limit has the 120° antiferromagnetic Néel ground state [59, 60] at $\nu = 1$, which spontaneously breaks the valley U(1) symmetry in our case and therefore, represents an intervalley-coherent state. The SDW in the 120° Néel state spontaneously breaks the moiré translational symmetry, and has an expanded unit cell with a period $\sqrt{3}a_M$. In Figs. 3(b) - 3(d), we show three types of SDW states, distinguished by their charge and spin patterns in the bottom layer. In SDW1 and SDW2, the holes in the bottom layer are mainly concentrated on MM sites. Both SDW1 and SDW2 have the 120° antiferromagnetic spin texture for holes on MM sites, but they differ by the spin vector chirality [49]. In SDW3, the holes in the bottom layer are redistributed in moiré superlattices such that the hole density on MM and XX sites have comparable magnitude; the corresponding spin texture is shown in Fig. 3(d). In addition, we also consider an FM_x state (also an intervalley coherent state), where the spin for holes in the bottom is polarized along an in-plane direction. We perform a self-consistent HF calculation for the SDW and FM_x states, compare their energies with the VP state, and obtain the phase diagram in Fig. 3(a) as a function of $V_{z\mathfrak{t}}$ and ϵ.

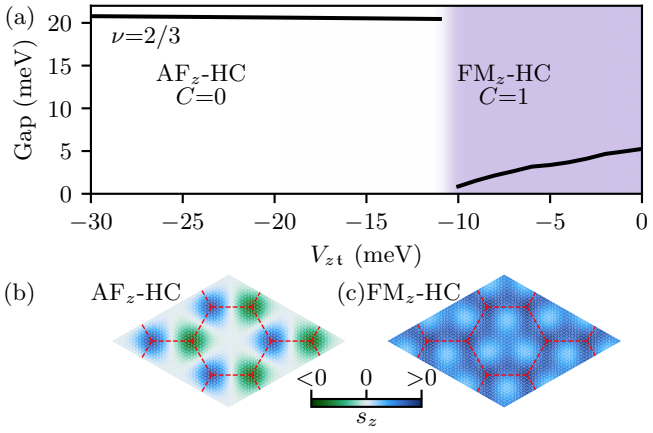


FIG. 4. (a) Interaction-induced phase diagram at $\nu = 2/3$ with $\epsilon = 17$, w=12 meV, and $V_{\mathfrak{b}}$=7 meV. Note that the sample-to-gate distance d has changed from 5 nm to 15 nm compared with other figures. The two competing phases are AF_z-HC and FM_z-HC, which respectively have AF_z and FM_z spin ordering on a generalized Wigner crystal with honeycomb lattice on the bottom layer. (b), (c) The spatial variation of the z component spin s_z on the bottom layer for AF_z-HC and FM_z-HC. The red dashed lines mark the emergent honeycomb lattice with a period of $\sqrt{3}a_M$ and vertices on MM sites.

In Fig. 3(e), we show the charge gap as a function of $V_{z\mathfrak{t}}$ at a fixed ϵ. As $V_{z\mathfrak{t}}$ increases from a large negative value toward 0, there is a first-order phase transition between the topologically trivial SDW phase and the topological VP ChI phase. Because the first-order phase transition breaks adiabatic continuity, the charge gap does not need to vanish at the transition point, and there can be a discontinuous jump in the gap. In contrast, the experimental charge gap [51] evolves *continuously* across the transition from a Mott insulator to a Chern insulator at $\nu = 1$, which could be due to disorder effects [61].

Topological charge density waves at $\nu = 2/3$.— Correlated insulators can develop not only at integer ν, but also at fractional ν, as demonstrated experimentally in Refs. 62–66. Here we focus on $\nu = 2/3$, where the Coulomb interaction can induce a charge density wave (CDW) state that forms a honeycomb lattice [67]. The enlarged unit cell has a period $\sqrt{3}a_M$ and contains three MM sites, but only two out of the three are occupied by holes in the bottom layer, which, therefore, leads to an effective honeycomb lattice. We theoretically find that the CDW state at $\nu = 2/3$ is sensitive to the long-range part of the Coulomb interaction, and can be energetically stabilized for $d = 15$ nm rather than $d = 5$ nm, where d is the sample-to-gate distance and controls the effective

range of the Coulomb interaction.

On the effective honeycomb lattice, there can be two types of spin ordering [67]: (1) antiferromagnetic (AF_z) order and (2) ferromagnetic (FM_z) order, where the spin polarization axis is out of the plane for both cases as illustrated respectively in Figs. 4(b) and 4(c). Here the FM_z state is also valley polarized. We perform self-consistent HF calculations respectively for the AF_z honeycomb (AF_z-HC) state and the FM_z honeycomb (FM_z-HC) state. Their energy competition gives rise to the $\nu = 2/3$ phase diagram in Fig. 4(a), where the AF_z-HC and FM_z-HC states are favorable respectively for $V_{z\mathfrak{t}}$ below and above a critical value. Remarkably, when the FM_z-HC state becomes energetically favorable, it is also topologically nontrivial with a quantized Chern number 1. Therefore, there can be a topological CDW state at $\nu = 2/3$. Here the topology emerges with a mechanism similar to that of the VP ChI state at $\nu = 1$, i.e., band inversion induced by $V_{z\mathfrak{t}}$.

Conclusion.— Our self-consistent theoretical results provide a reasonable qualitative understanding of the field-induced topological states in Ref. 51. The theory sets up a general framework to study topological interaction effects in a transition metal dichalcogenide based moiré system, and can be readily applied to study a variety of interaction-induced symmetry breaking phases [49, 62, 67–72]. For AB-stacked $MoTe_2/WSe_2$, many future directions can be explored in both theory and experiment. The $\nu = 1$ Chern insulator has spontaneous VP, but does *not* break any *continuous* symmetry. It is an Ising-type ordering with a finite Curie temperature, which could be theoretically estimated by studying the valley magnon and domain fluctuations [73]. This VP state can result in interesting optical phenomena, for example, Faraday and Kerr rotations [74]. The multiple distinct quantum phases (SDW, ChI, and $\mathbb{Z}_2$ topological insulators) that emerge in a single system can be used as building blocks to design new quantum phases on demand. For example, by introducing proximitized superconductivity, an interface between the $\nu = 1$ SDW state and the $\nu = 2$ $\mathbb{Z}_2$ topological insulator could host Majorana zero modes.

This work is supported by the National Key R&D Program of China 2021YFA1401300 (F. W.) and the Laboratory for Physical Sciences (work at Maryland). We thank the University of Maryland High-Performance Computing Cluster (HPCC) for providing computational resources. F. W. also acknowledges support by startup funding from Wuhan University.

* wufcheng@whu.edu.cn

[1] K. von Klitzing, G. Dorda, and M. Pepper, New Method for High-Accuracy Determination of the Fine-Structure Constant Based on Quantized Hall Resistance, Phys. Rev. Lett. **45**, 494 (1980).
[2] D. J. Thouless, M. Kohmoto, M. P. Nightingale, and M. den Nijs, Quantized Hall Conductance in a Two-Dimensional Periodic Potential, Phys. Rev. Lett. **49**, 405 (1982).
[3] Q. Niu, D. J. Thouless, and Y.-S. Wu, Quantized Hall conductance as a topological invariant, Phys. Rev. B **31**, 3372 (1985).
[4] F. D. M. Haldane, Model for a Quantum Hall Effect without Landau Levels: Condensed-Matter Realization of the "Parity Anomaly", Phys. Rev. Lett. **61**, 2015 (1988).
[5] C. L. Kane and E. J. Mele, Quantum Spin Hall Effect in Graphene, Phys. Rev. Lett. **95**, 226801 (2005).
[6] M. Onoda and N. Nagaosa, Quantized Anomalous Hall Effect in Two-Dimensional Ferromagnets: Quantum Hall Effect in Metals, Phys. Rev. Lett. **90**, 206601 (2003).
[7] X.-L. Qi, Y.-S. Wu, and S.-C. Zhang, Topological quantization of the spin Hall effect in two-dimensional paramagnetic semiconductors, Phys. Rev. B **74**, 085308 (2006).
[8] X.-L. Qi, T. L. Hughes, and S.-C. Zhang, Topological field theory of time-reversal invariant insulators, Phys. Rev. B **78**, 195424 (2008).
[9] C.-X. Liu, X.-L. Qi, X. Dai, Z. Fang, and S.-C. Zhang, Quantum Anomalous Hall Effect in $Hg_{1-y}Mn_yTe$ Quantum Wells, Phys. Rev. Lett. **101**, 146802 (2008).
[10] R. Yu, W. Zhang, H.-J. Zhang, S.-C. Zhang, X. Dai, and Z. Fang, Quantized Anomalous Hall Effect in Magnetic Topological Insulators, Science **329**, 61 (2010).
[11] Z. Qiao, S. A. Yang, W. Feng, W.-K. Tse, J. Ding, Y. Yao, J. Wang, and Q. Niu, Quantum anomalous Hall effect in graphene from Rashba and exchange effects, Phys. Rev. B **82**, 161414 (2010).
[12] K. Nomura and N. Nagaosa, Surface-Quantized Anomalous Hall Current and the Magnetoelectric Effect in Magnetically Disordered Topological Insulators, Phys. Rev. Lett. **106**, 166802 (2011).
[13] D. Zhang, M. Shi, T. Zhu, D. Xing, H. Zhang, and J. Wang, Topological Axion States in the Magnetic Insulator $MnBi_2Te_4$ with the Quantized Magnetoelectric Effect, Phys. Rev. Lett. **122**, 206401 (2019).
[14] J. Li, Y. Li, S. Du, Z. Wang, B.-L. Gu, S.-C. Zhang, K. He, W. Duan, and Y. Xu, Intrinsic magnetic topological insulators in van der Waals layered MnBi2Te4-family materials, Science Advances **5**, eaaw5685 (2019).
[15] M. M. Otrokov, I. I. Klimovskikh, H. Bentmann, D. Estyunin, A. Zeugner, Z. S. Aliev, S. Gaß, A. U. B. Wolter, A. V. Koroleva, A. M. Shikin, M. Blanco-Rey, M. Hoffmann, I. P. Rusinov, A. Y. Vyazovskaya, S. V. Eremeev, Y. M. Koroteev, V. M. Kuznetsov, F. Freyse, J. Sánchez-Barriga, I. R. Amiraslanov, M. B. Babanly, N. T. Mamedov, N. A. Abdullayev, V. N. Zverev, A. Alfonsov, V. Kataev, B. Büchner, E. F. Schwier, S. Kumar, A. Kimura, L. Petaccia, G. Di Santo, R. C. Vidal, S. Schatz, K. Kißner, M. Ünzelmann, C. H. Min, S. Moser, T. R. F. Peixoto, F. Reinert, A. Ernst, P. M. Echenique, A. Isaeva, and E. V. Chulkov, Prediction and observation of an antiferromagnetic topological insulator, Nature **576**, 416 (2019).
[16] C. Liu, T. L. Hughes, X.-L. Qi, K. Wang, and S.-C. Zhang, Quantum Spin Hall Effect in Inverted Type-II Semiconductors, Phys. Rev. Lett. **100**, 236601 (2008).
[17] Y.-H. Zhang, D. Mao, Y. Cao, P. Jarillo-Herrero, and T. Senthil, Nearly flat Chern bands in moiré superlat-

tices, Phys. Rev. B **99**, 075127 (2019).
[18] B. A. Bernevig and S.-C. Zhang, Quantum Spin Hall Effect, Phys. Rev. Lett. **96**, 106802 (2006).
[19] D. N. Sheng, Z. Y. Weng, L. Sheng, and F. D. M. Haldane, Quantum Spin-Hall Effect and Topologically Invariant Chern Numbers, Phys. Rev. Lett. **97**, 036808 (2006).
[20] X. Qian, J. Liu, L. Fu, and J. Li, Quantum spin Hall effect in two-dimensional transition metal dichalcogenides, Science **346**, 1344 (2014).
[21] C.-Z. Chang, J. Zhang, X. Feng, J. Shen, Z. Zhang, M. Guo, K. Li, Y. Ou, P. Wei, L.-L. Wang, Z.-Q. Ji, Y. Feng, S. Ji, X. Chen, J. Jia, X. Dai, Z. Fang, S.-C. Zhang, K. He, Y. Wang, L. Lu, X.-C. Ma, and Q.-K. Xue, Experimental Observation of the Quantum Anomalous Hall Effect in a Magnetic Topological Insulator, Science **340**, 167 (2013).
[22] Y.-F. Zhao, R. Zhang, R. Mei, L.-J. Zhou, H. Yi, Y.-Q. Zhang, J. Yu, R. Xiao, K. Wang, N. Samarth, M. H. W. Chan, C.-X. Liu, and C.-Z. Chang, Tuning the Chern number in quantum anomalous Hall insulators, Nature **588**, 419 (2020).
[23] Y. Deng, Y. Yu, M. Z. Shi, Z. Guo, Z. Xu, J. Wang, X. H. Chen, and Y. Zhang, Quantum anomalous Hall effect in intrinsic magnetic topological insulator MnBi2Te4, Science **367**, 895 (2020).
[24] C. Liu, Y. Wang, H. Li, Y. Wu, Y. Li, J. Li, K. He, Y. Xu, J. Zhang, and Y. Wang, Robust axion insulator and Chern insulator phases in a two-dimensional antiferromagnetic topological insulator, Nat. Mater. **19**, 522 (2020).
[25] A. L. Sharpe, E. J. Fox, A. W. Barnard, J. Finney, K. Watanabe, T. Taniguchi, M. A. Kastner, and D. Goldhaber-Gordon, Emergent ferromagnetism near three-quarters filling in twisted bilayer graphene, Science **365**, 605 (2019).
[26] M. Serlin, C. L. Tschirhart, H. Polshyn, Y. Zhang, J. Zhu, K. Watanabe, T. Taniguchi, L. Balents, and A. F. Young, Intrinsic quantized anomalous Hall effect in a moiré heterostructure, Science **367**, 900 (2020).
[27] G. Chen, A. L. Sharpe, E. J. Fox, Y.-H. Zhang, S. Wang, L. Jiang, B. Lyu, H. Li, K. Watanabe, T. Taniguchi, Z. Shi, T. Senthil, D. Goldhaber-Gordon, Y. Zhang, and F. Wang, Tunable correlated Chern insulator and ferromagnetism in a moiré superlattice, Nature **579**, 56 (2020).
[28] H. Polshyn, J. Zhu, M. A. Kumar, Y. Zhang, F. Yang, C. L. Tschirhart, M. Serlin, K. Watanabe, T. Taniguchi, A. H. MacDonald, and A. F. Young, Electrical switching of magnetic order in an orbital Chern insulator, Nature **588**, 66 (2020).
[29] H. Polshyn, Y. Zhang, M. A. Kumar, T. Soejima, P. Ledwith, K. Watanabe, T. Taniguchi, A. Vishwanath, M. P. Zaletel, and A. F. Young, Topological charge density waves at half-integer filling of a moiré superlattice, Nat. Phys. **18**, 42 (2022).
[30] M. König, S. Wiedmann, C. Brüne, A. Roth, H. Buhmann, L. W. Molenkamp, X.-L. Qi, and S.-C. Zhang, Quantum Spin Hall Insulator State in HgTe Quantum Wells, Science **318**, 766 (2007).
[31] I. Knez, R. R. Du, and G. Sullivan, Finite conductivity in mesoscopic Hall bars of inverted InAs/GaSb quantum wells, Phys. Rev. B **81**, 201301 (2010).
[32] I. Knez, R.-R. Du, and G. Sullivan, Evidence for Helical Edge Modes in Inverted InAs/GaSb Quantum Wells, Phys. Rev. Lett. **107**, 136603 (2011).
[33] Z. Fei, T. Palomaki, S. Wu, W. Zhao, X. Cai, B. Sun, P. Nguyen, J. Finney, X. Xu, and D. H. Cobden, Edge conduction in monolayer WTe2, Nature Phys **13**, 677 (2017).
[34] S. Wu, V. Fatemi, Q. D. Gibson, K. Watanabe, T. Taniguchi, R. J. Cava, and P. Jarillo-Herrero, Observation of the quantum spin Hall effect up to 100 kelvin in a monolayer crystal, Science **359**, 76 (2018).
[35] Y. Cao, V. Fatemi, A. Demir, S. Fang, S. L. Tomarken, J. Y. Luo, J. D. Sanchez-Yamagishi, K. Watanabe, T. Taniguchi, E. Kaxiras, R. C. Ashoori, and P. Jarillo-Herrero, Correlated insulator behaviour at half-filling in magic-angle graphene superlattices, Nature **556**, 80 (2018).
[36] Y. Cao, V. Fatemi, S. Fang, K. Watanabe, T. Taniguchi, E. Kaxiras, and P. Jarillo-Herrero, Unconventional superconductivity in magic-angle graphene superlattices, Nature **556**, 43 (2018).
[37] M. Yankowitz, S. Chen, H. Polshyn, Y. Zhang, K. Watanabe, T. Taniguchi, D. Graf, A. F. Young, and C. R. Dean, Tuning superconductivity in twisted bilayer graphene, Science **363**, 1059 (2019).
[38] G. Chen, L. Jiang, S. Wu, B. Lyu, H. Li, B. L. Chittari, K. Watanabe, T. Taniguchi, Z. Shi, J. Jung, Y. Zhang, and F. Wang, Evidence of Gate-Tunable Mott Insulator in Trilayer Graphene-Boron Nitride Moiré Superlattice, Nat. Phys. **15**, 237 (2019).
[39] Y. Cao, D. Rodan-Legrain, O. Rubies-Bigorda, J. M. Park, K. Watanabe, T. Taniguchi, and P. Jarillo-Herrero, Tunable correlated states and spin-polarized phases in twisted bilayer–bilayer graphene, Nature **583**, 215 (2020).
[40] S. Chen, M. He, Y.-H. Zhang, V. Hsieh, Z. Fei, K. Watanabe, T. Taniguchi, D. H. Cobden, X. Xu, C. R. Dean, and M. Yankowitz, Electrically tunable correlated and topological states in twisted monolayer–bilayer graphene, Nature Physics **17**, 374 (2020).
[41] D. Wong, K. P. Nuckolls, M. Oh, B. Lian, Y. Xie, S. Jeon, K. Watanabe, T. Taniguchi, B. A. Bernevig, and A. Yazdani, Cascade of electronic transitions in magic-angle twisted bilayer graphene, Nature **582**, 198 (2020).
[42] X. Lu, P. Stepanov, W. Yang, M. Xie, M. A. Aamir, I. Das, C. Urgell, K. Watanabe, T. Taniguchi, G. Zhang, A. Bachtold, A. H. MacDonald, and D. K. Efetov, Superconductors, orbital magnets and correlated states in magic-angle bilayer graphene, Nature **574**, 653 (2019).
[43] C. Shen, Y. Chu, Q. Wu, N. Li, S. Wang, Y. Zhao, J. Tang, J. Liu, J. Tian, K. Watanabe, T. Taniguchi, R. Yang, Z. Y. Meng, D. Shi, O. V. Yazyev, and G. Zhang, Correlated states in twisted double bilayer graphene, Nat. Phys. **16**, 520 (2020).
[44] Y. Choi, J. Kemmer, Y. Peng, A. Thomson, H. Arora, R. Polski, Y. Zhang, H. Ren, J. Alicea, G. Refael, F. von Oppen, K. Watanabe, T. Taniguchi, and S. Nadj-Perge, Electronic correlations in twisted bilayer graphene near the magic angle, Nat. Phys. **15**, 1174 (2019).
[45] Y. Xie, B. Lian, B. Jäck, X. Liu, C.-L. Chiu, K. Watanabe, T. Taniguchi, B. A. Bernevig, and A. Yazdani, Spectroscopic signatures of many-body correlations in magic-angle twisted bilayer graphene, Nature **572**, 101 (2019).
[46] G. Chen, A. L. Sharpe, P. Gallagher, I. T. Rosen, E. J. Fox, L. Jiang, B. Lyu, H. Li, K. Watanabe, T. Taniguchi,

J. Jung, Z. Shi, D. Goldhaber-Gordon, Y. Zhang, and F. Wang, Signatures of tunable superconductivity in a trilayer graphene moiré superlattice, Nature **572**, 215 (2019).
[47] X. Liu, Z. Hao, E. Khalaf, J. Y. Lee, Y. Ronen, H. Yoo, D. Haei Najafabadi, K. Watanabe, T. Taniguchi, A. Vishwanath, and P. Kim, Tunable spin-polarized correlated states in twisted double bilayer graphene, Nature **583**, 221 (2020).
[48] F. Wu, T. Lovorn, E. Tutuc, I. Martin, and A. H. MacDonald, Topological insulators in twisted transition metal dichalcogenide homobilayers, Phys. Rev. Lett. **122**, 086402 (2019).
[49] H. Pan, F. Wu, and S. Das Sarma, Band topology, Hubbard model, Heisenberg model, and Dzyaloshinskii-Moriya interaction in twisted bilayer WSe_2, Phys. Rev. Research **2**, 033087 (2020).
[50] T. Devakul, V. Crépel, Y. Zhang, and L. Fu, Magic in twisted transition metal dichalcogenide bilayers, Nat Commun **12**, 6730 (2021).
[51] T. Li, S. Jiang, B. Shen, Y. Zhang, L. Li, Z. Tao, T. Devakul, K. Watanabe, T. Taniguchi, L. Fu, J. Shan, and K. F. Mak, Quantum anomalous Hall effect from intertwined moiré bands, Nature **600**, 641 (2021).
[52] Y.-M. Xie, C.-P. Zhang, J.-X. Hu, K. F. Mak, and K. T. Law, Valley-Polarized Quantum Anomalous Hall State in Moiré $MoTe_2/WSe_2$ Heterobilayers, Phys. Rev. Lett. **128**, 026402 (2022).
[53] Y. Zhang, T. Devakul, and L. Fu, Spin-textured Chern bands in AB-stacked transition metal dichalcogenide bilayers, PNAS **118**, 10.1073/pnas.2112673118 (2021).
[54] T. Devakul and L. Fu, Quantum anomalous Hall effect from inverted charge transfer gap, arXiv:2109.13909 (2021).
[55] See supplemental Material, which include [56–58].
[56] F. Wu and S. Das Sarma, Quantum geometry and stability of moiré flatband ferromagnetism, Phys. Rev. B **102**, 165118 (2020).
[57] T. Fukui, Y. Hatsugai, and H. Suzuki, Chern Numbers in Discretized Brillouin Zone: Efficient Method of Computing (Spin) Hall Conductances, J. Phys. Soc. Jpn. **74**, 1674 (2005).
[58] H. J. Monkhorst and J. D. Pack, Special points for Brillouin-zone integrations, Phys. Rev. B **13**, 5188 (1976).
[59] F. Wu, T. Lovorn, E. Tutuc, and A. H. MacDonald, Hubbard model physics in transition metal dichalcogenide moiré bands, Phys. Rev. Lett. **121**, 026402 (2018).
[60] N. C. Hu and A. H. MacDonald, Competing magnetic states in transition metal dichalcogenide moiré materials, Phys. Rev. B **104**, 214403 (2021).
[61] S. Ahn and S. Das Sarma, Disorder-induced two-dimensional metal-insulator transition in moiré transition metal dichalcogenide multilayers, Phys. Rev. B **105**, 115114 (2022).
[62] Y. Xu, S. Liu, D. A. Rhodes, K. Watanabe, T. Taniguchi, J. Hone, V. Elser, K. F. Mak, and J. Shan, Correlated insulating states at fractional fillings of moiré superlattices, Nature **587**, 214 (2020).
[63] H. Li, S. Li, E. C. Regan, D. Wang, W. Zhao, S. Kahn, K. Yumigeta, M. Blei, T. Taniguchi, K. Watanabe, S. Tongay, A. Zettl, M. F. Crommie, and F. Wang, Imaging two-dimensional generalized Wigner crystals, Nature **597**, 650 (2021).
[64] E. Liu, T. Taniguchi, K. Watanabe, N. M. Gabor, Y.-T. Cui, and C. H. Lui, Excitonic and Valley-Polarization Signatures of Fractional Correlated Electronic Phases in a WSe_2/WS_2 Moiré Superlattice, Phys. Rev. Lett. **127**, 037402 (2021).
[65] E. C. Regan, D. Wang, C. Jin, M. I. Bakti Utama, B. Gao, X. Wei, S. Zhao, W. Zhao, Z. Zhang, K. Yumigeta, M. Blei, J. D. Carlström, K. Watanabe, T. Taniguchi, S. Tongay, M. Crommie, A. Zettl, and F. Wang, Mott and generalized Wigner crystal states in WSe_2/WS_2 moiré superlattices, Nature **579**, 359 (2020).
[66] Y. Zhou, J. Sung, E. Brutschea, I. Esterlis, Y. Wang, G. Scuri, R. J. Gelly, H. Heo, T. Taniguchi, K. Watanabe, G. Zaránd, M. D. Lukin, P. Kim, E. Demler, and H. Park, Bilayer Wigner crystals in a transition metal dichalcogenide heterostructure, Nature **595**, 48 (2021).
[67] H. Pan, F. Wu, and S. Das Sarma, Quantum phase diagram of a Moiré-Hubbard model, Phys. Rev. B **102**, 201104 (2020).
[68] L. Wang, E.-M. Shih, A. Ghiotto, L. Xian, D. A. Rhodes, C. Tan, M. Claassen, D. M. Kennes, Y. Bai, B. Kim, K. Watanabe, T. Taniguchi, X. Zhu, J. Hone, A. Rubio, A. N. Pasupathy, and C. R. Dean, Correlated electronic phases in twisted bilayer transition metal dichalcogenides, Nature Materials **19**, 861 (2020).
[69] J. Gu, L. Ma, S. Liu, K. Watanabe, T. Taniguchi, J. C. Hone, J. Shan, and K. F. Mak, Dipolar excitonic insulator in a moire lattice, arXiv:2108.06588 (2021).
[70] Z. Zhang, E. C. Regan, D. Wang, W. Zhao, S. Wang, M. Sayyad, K. Yumigeta, K. Watanabe, T. Taniguchi, S. Tongay, M. Crommie, A. Zettl, M. P. Zaletel, and F. Wang, Correlated interlayer exciton insulator in double layers of monolayer WSe_2 and moiré WS_2/WSe_2, arXiv:2108.07131 (2021).
[71] H. Pan and S. Das Sarma, Interaction-Driven Filling-Induced Metal-Insulator Transitions in 2D Moiré Lattices, Phys. Rev. Lett. **127**, 096802 (2021).
[72] H. Pan and S. Das Sarma, Interaction range and temperature dependence of symmetry breaking in strongly correlated two-dimensional moiré transition metal dichalcogenide bilayers, Phys. Rev. B **105**, 041109 (2022).
[73] F. Wu and S. Das Sarma, Collective Excitations of Quantum Anomalous Hall Ferromagnets in Twisted Bilayer Graphene, Phys. Rev. Lett. **124**, 046403 (2020).
[74] W.-K. Tse and A. H. MacDonald, Giant Magneto-Optical Kerr Effect and Universal Faraday Effect in Thin-Film Topological Insulators, Phys. Rev. Lett. **105**, 057401 (2010).